Arbitrary-order Hilbert spectral analysis for time series possessing scaling statistics: Comparison study with detrended fluctuation analysis and wavelet leaders

Y. X. Huang (黄永祥),[1,2,3,4,5,6,7,*] F. G. Schmitt,[4,5,6,†] J.-P. Hermand,[7] Y. Gagne,[8] Z. M. Lu (卢志明),[1,2,3] and Y. L. Liu (刘宇陆)[1,2]

[1]*Shanghai Institute of Applied Mathematics and Mechanics, Shanghai University, Shanghai 200072, China*
[2]*Shanghai Key Laboratory of Mechanics in Energy and Environment Engineering, Yanchang Road, Shanghai 200072, China*
[3]*E-Institutes of Shanghai Universities, Shanghai University, Shanghai 200072, China*
[4]*Université Lille Nord de France, F-59044 Lille, France*
[5]*USTL, LOG, F-62930 Wimereux, France*
[6]*CNRS, UMR 8187, F-62930 Wimereux, France*
[7]*Environmental Hydroacoustics Laboratory, Université Libre de Bruxelles, Avenue F-D. Roosevelt 50-CP 194/5, B-1050 Brussels, Belgium*
[8]*LEGI, CNRS/UJF/INPG, UMR 5519, F-38041 Grenoble, France*

(Received 27 January 2011; published 14 July 2011)

In this paper we present an extended version of Hilbert-Huang transform, namely arbitrary-order Hilbert spectral analysis, to characterize the scale-invariant properties of a time series directly in an amplitude-frequency space. We first show numerically that due to a nonlinear distortion, traditional methods require high-order harmonic components to represent nonlinear processes, except for the Hilbert-based method. This will lead to an artificial energy flux from the low-frequency (large scale) to the high-frequency (small scale) part. Thus the power law, if it exists, is contaminated. We then compare the Hilbert method with structure functions (SF), detrended fluctuation analysis (DFA), and wavelet leader (WL) by analyzing fractional Brownian motion and synthesized multifractal time series. For the former simulation, we find that all methods provide comparable results. For the latter simulation, we perform simulations with an intermittent parameter $\mu = 0.15$. We find that the SF underestimates scaling exponent when $q > 3$. The Hilbert method provides a slight underestimation when $q > 5$. However, both DFA and WL overestimate the scaling exponents when $q > 5$. It seems that Hilbert and DFA methods provide better singularity spectra than SF and WL. We finally apply all methods to a passive scalar (temperature) data obtained from a jet experiment with a Taylor's microscale Reynolds number $\mathrm{Re}_\lambda \simeq 250$. Due to the presence of strong ramp-cliff structures, the SF fails to detect the power law behavior. For the traditional method, the ramp-cliff structure causes a serious artificial energy flux from the low-frequency (large scale) to the high-frequency (small scale) part. Thus DFA and WL underestimate the scaling exponents. However, the Hilbert method provides scaling exponents $\xi_\theta(q)$ quite close to the one for longitudinal velocity, indicating a less intermittent passive scalar field than what was believed before.

DOI: 10.1103/PhysRevE.84.016208 PACS number(s): 05.45.Tp, 02.50.Fz, 94.05.Lk

I. INTRODUCTION

Multifractal properties have been found in many fields, such as turbulence [1–3], rainfall [4–7], financial time series [8–11], physiology [12], etc. Conventionally, multifractal properties of such time series are characterized by the scaling exponents $\zeta(q)$, which are extracted by structure function (SF) analysis: $\Delta V_\ell^q \sim \ell^{\zeta(q)}$, where $\Delta V_\ell = |V(x+\ell) - V(x)|$ are the increment for scale separation ℓ, and $\zeta(q)$ is a nonlinear function [1,2,13]. The function $\zeta(q)$ is linear for monoscaling processes and nonlinear for multifractal processes. We may also mention the detrended fluctuation analysis (DFA) [14–16] or the multifractal detrended fluctuation analysis [17], which are sometimes also employed for scaling time series analysis. The DFA method is similar to SFs since it involves increments and characterizes the scale invariance in the physical domain.

Other widely used methods are wavelet-based methods, for example, wavelet transform modulus maxima (WTMM), wavelet leader (WL), or gradient modulus wavelet projection (GMWP), to extract the scaling exponents from a scaling time series [18–30]. However, as we will show in this paper, the wavelets share the same drawback with Fourier transform, which requires high-order harmonic components to represent nonlinear processes.

Some of us have proposed recently a new methodology, namely arbitrary-order Hilbert spectral analysis (HSA), to characterize the scale-invariant properties directly in amplitude-frequency space [31–33]. It is an extended version of the Hilbert-Huang transform (HHT), which provides a joint probability density function (pdf) in an amplitude-frequency space [31,33]. We have applied part of this new methodology to several different time series to show its efficiency and validity: turbulence experimental database [31], synthesized fractional Brownian motion (fBm) time series [32], surf zone marine turbulence data [34], and river flow discharge data [35]. In this paper we consider in length and precisely this new method and its validation and calibration. We first introduce this new methodology in detail. We then validate and calibrate it by analyzing a synthesized multifractal time series. We finally consider a passive scalar (temperature) data set with strong ramp-cliff structures. Due to the presence of ramp-cliff structures, the classical SF analysis fails to detect the power law behavior [36]. Additionally, for traditional methods, such as Fourier transform, wavelet transform, high-order harmonics is

*yongxianghuang@gmail.com
†francois.schmitt@univ-lille1.fr

required to represent these structures and leads to an artificial energy flux from the large-scale part (low frequency) to the small-scale part (high frequency) [36].

This paper is organized as follows. We present the definition of the arbitrary-order Hilbert spectral analysis in Sec. II. The classical structure function analysis, multifractal detrended fluctuation analysis, and wavelet leader are also presented in this section. We then consider a nonlinear effect by using the classical Duffing equation to show the artificial high-order harmonic components required by the classical methods, for example, Fourier transform and wavelet transform, in Sec. III. In Sec. IV we perform a comparison study of the arbitrary-order HSA with other methods by analyzing a fBm simulation and a synthesized multifractal time series. We then present in Sec. V an analysis of real temperature data obtained from a jet experiment. We finally draw the main conclusions in Sec. VI.

II. METHODOLOGY

A. Arbitrary-order Hilbert spectral analysis

1. *Empirical mode decomposition*

The most innovative part of the Hilbert-Huang transform is the so-called empirical mode decomposition (EMD). In the real world most of the signals are multicomponents, which means that different scales can coexist simultaneously [37–39]. This may be considered as fast oscillations superposed to slower ones at a local level [40,41]. Meanwhile, for decomposition methods, a characteristic scale (CS) is always defined implicitly or explicitly before the decomposition. For example, the CS of the classical Fourier analysis is a period of sine wave. The CS of wavelet transform is the shape of the mother wavelet [33]. In the present method, the CS is defined as the distance between two successive maxima (respectively, minima) points. Then the so-called intrinsic mode functions (IMF) are proposed to represent each mono-component signal. An IMF satisfies the following two conditions: (i) the difference between the number of local extrema and the number of zero crossings must be zero or one; (ii) the running mean value of the envelope defined by the local maxima and the envelope defined by the local minima is zero [38,39].

A subpart of the EMD algorithm, called "sifting process," is then designed to decompose a given signal into several IMF modes [38–40]. The first step of the sifting process is to identify all the local maxima (respectively, minima) points for a given time series $x(t)$. Once all the local extrema points are identified, the upper envelope $e_{\max}(t)$ and the lower envelope $e_{\min}(t)$ are constructed, respectively, for the local maxima and minima points by using a cubic spline algorithm. The mean between these two envelopes is defined as

$$m_1(t) = \frac{e_{\max}(t) + e_{\min}(t)}{2}. \tag{1}$$

Thus the first component is estimated by

$$h_1(t) = x(t) - m_1(t). \tag{2}$$

Ideally, $h_1(t)$ should be an IMF as expected. However, $h_1(t)$ may not satisfy the above-mentioned conditions to be an IMF. The function $h_1(t)$ is then taken as a new time series and this sifting process is repeated j times, until $h_{1j}(t)$ is an IMF:

$$h_{1j}(t) = h_{1(j-1)}(t) - m_{1j}(t). \tag{3}$$

The first IMF component $C_1(t)$ is then written as

$$C_1(t) = h_{1j}(t), \tag{4}$$

and the residual $r_1(t)$ as

$$r_1(t) = x(t) - C_1(t), \tag{5}$$

from the data $x(t)$. The sifting procedure is then repeated on the residual until $r_n(t)$ becomes a monotonic function or at most has one local extreme point, which means that no more IMF can be extracted from $r_n(t)$. There are finally $n-1$ IMF modes with one residual $r_n(t)$. The original signal $x(t)$ is rewritten at the end of the process as

$$x(t) = \sum_{i=1}^{n-1} C_i(t) + r_n(t). \tag{6}$$

To guarantee that the IMF modes retain enough physical sense, a certain stopping criterion has to be introduced to stop the sifting process properly. Different types of stopping criteria have been introduced by several authors [38–40,42,43]. The first stopping criterion is a Cauchy-type convergence criterion. We introduce the standard deviation (SD), defined for two successive sifting processes as

$$\mathrm{SD} = \frac{\sum_{t=0}^{T} |h_{i(j-1)}(t) - h_j(t)|^2}{\sum_{t=0}^{T} h_{i(j-1)}^2(t)}. \tag{7}$$

If a calculated SD is smaller than a given value, then the sifting stops, and gives an IMF. A typical value is $0.2 \sim 0.3$, proposed based on Huang *et al.*'s experiences [38,39]. Another widely used criterion is based on three thresholds: α, θ_1, and θ_2, which are designed to guarantee globally small fluctuations, meanwhile taking into account locally large excursions [40]. The mode amplitude and evaluation function are given as

$$a(t) = \frac{e_{\max}(t) - e_{\min}(t)}{2}, \tag{8a}$$

and

$$\sigma(t) = |m(t)/a(t)|. \tag{8b}$$

So that the sifting is iterated until $\sigma(t) < \theta_1$ for some prescribed fraction $1-\alpha$ of the total duration, while $\sigma(t) < \theta_2$ for the remaining fraction. The typical values proposed by Rilling *et al.* [40] are $\alpha \approx 0.05$, $\theta_1 \approx 0.05$, and $\theta_2 \approx 10\,\theta_1$, respectively, based on their experience. In our practice, if one of these criteria is satisfied, then the sifting process will stop. We also set a maximal iteration number (e.g., 300) to avoid over-decomposing the time series.

The above-described EMD algorithm performs the decomposition on a very local level in the physical domain without *a priori* basis. This means that the present decomposition is *a posteriori*: The basis is induced by the data itself [38,39,41]. It is thus a scale-based decomposition. Since its introduction, this method has attracted large interests in various research fields: waves [34,44,45], biological applications [46–48], financial studies [49], meteorology and climate studies [35,50–54],

mechanical engineering [55,56], acoustics [57], aquatic environment [58], and turbulence [31], to quote a few. More detail about the EMD algorithm can be found in several methodological papers [38–41,43,59].

2. *Hilbert spectral analysis*

After having extracted the IMF modes, one can apply the associated Hilbert spectral analysis to each component C_i in order to extract the energy time-frequency information from the data [38,39,60]. The Hilbert transform of a function $C(t)$ is written as

$$\tilde{C}(t) = \frac{1}{\pi} P \int \frac{C(t')}{t - t'} dt', \tag{9}$$

where P means the Cauchy principle value [37,38,60,61]. For each mode function $C_i(t)$, one can then construct the analytical signal [37,61], $\mathbb{C}_i(t)$, as

$$\mathbb{C}_i(t) = C_i(t) + j\tilde{C}_i(t) = \mathcal{A}_i(t)\, e^{j\theta_i(t)}, \tag{10}$$

where

$$\begin{aligned} \mathcal{A}_i(t) &= [C_i(t)^2 + \tilde{C}_i^2(t)]^{1/2} \\ \theta_i(t) &= \arctan\left(\tfrac{\tilde{C}_i(t)}{C_i(t)}\right). \end{aligned} \tag{11}$$

Hence the instantaneous frequency is defined as

$$\omega_i = \frac{1}{2\pi} \frac{d\theta_i(t)}{dt}. \tag{12}$$

The original signal is finally represented [excluding the residual $r_n(t)$] as

$$x(t) = \mathrm{Re} \sum_{i=1}^{N} \mathcal{A}_i(t) e^{j\theta_i(t)} = \mathrm{Re} \sum_{i=1}^{N} \mathcal{A}_i(t) e^{j\int \omega_i(t) dt}, \tag{13}$$

where here "Re" means real part. The above procedure is the classical Hilbert spectral analysis [37,61]. The combination of EMD and HSA is thus called Hilbert-Huang transform by some authors [43]. The Hilbert-Huang transform can be taken as a generalization of the Fourier transform, since it allows frequency modulation and amplitude modulation simultaneously. The Hilbert spectrum, $H(\omega,t) = \mathcal{A}^2(\omega,t)$, is designed to represent the energy in a time-frequency representation [60]. We further can define the Hilbert marginal spectrum as

$$h(\omega) = \int_0^{+\infty} H(\omega,t)\, dt. \tag{14}$$

This is similar with the Fourier spectrum, and can be interpreted as the energy associated with each frequency. However, we underline the fact that the definition of frequency here is different from the definition in the Fourier frame. Thus the interpretation of the Hilbert marginal spectrum should be given more caution [38,39].

3. *Arbitrary-order Hilbert spectral analysis*

We can also define the joint pdf $p(\omega,\mathcal{A})$ of the instantaneous frequency ω and the amplitude $\mathcal{A}$ for each of these IMF modes [31–33,60]. The Hilbert marginal spectrum Eq. (14) is then rewritten as

$$h(\omega) = \int_0^{+\infty} p(\omega,\mathcal{A})\mathcal{A}^2 d\mathcal{A}. \tag{15}$$

The above definition is no more than the second-order statistical moment. This constatation has led some of us to recently generalize this approach to arbitrary-order moment $q \geqslant 0$ [31–33]:

$$\mathcal{L}_q(\omega) = \int_0^{+\infty} p(\omega,\mathcal{A})\mathcal{A}^q d\mathcal{A}. \tag{16}$$

In case of scale invariance, we have

$$\mathcal{L}_q(\omega) \sim \omega^{-\xi(q)}, \tag{17}$$

in which $\xi(q)$ is the Hilbert-based scaling exponent function. Due to the integration operator, $\xi(q) - 1$ can be associated with $\zeta(q)$ from SF analysis [31,33].

A limitation of the Hilbert-based method we proposed here is that it lacks the ability to consider $q < 0$.[1] In other words, similarly with the SF analysis, it has no resolution on the right part of the singularity spectrum. The main drawback of the Hilbert-based method is its absence of solid theoretical ground, since the EMD part is almost empirical [43]. It has been found experimentally that the method, especially for the HSA, is statistically stable with different stopping criteria [42]. Recently, Flandrin *et al.* have obtained new theoretical results on the EMD method [41,59,62–64]. However, more theoretical work is still needed to fully mathematically understand this method.

B. Structure function analysis

The conventional way to extract scaling exponents is the classical SF analysis, which has been proposed in the field of turbulence and is now quite classical for intermittency studies [13]. The qth order SF is written as

$$S_q(\ell) = \langle |\Delta x_\ell(t)|^q \rangle \sim \ell^{\zeta(q)}, \tag{18}$$

where $\Delta x_\ell(t) = x(t+\ell) - x(t)$ and ℓ is the time separation. The scaling exponent $\zeta(q)$ characterizes the fluctuation statistic at all scales; it is linear for monofractal processes such as fractional Brownian motion, and nonlinear and concave (as a second Laplace characteristic function) for multifractal processes [65]. This approach has been widely used in turbulent research [1,2,13] and also other research fields [9,66,67]. However, the increment operation acts a filter and thus SF characterizes the scale-invariant properties in an indirect way; see detailed discussion in Refs. [33,36].

As we have shown elsewhere, the increment operation in SF acts a filter and is a global operation. It thus measures the scale-invariant property in an indirect way. It is also found that it is strongly influenced by energetic large-scale structures [33,36]. Therefore the SF analysis is not suitable for those data which possess energetic large-scale structures. We will show an example of passive scalar turbulence data with strong

[1] In fact, Eq. (16) converges when $q \geqslant -1$. However, in practice, we only consider the case $q \geqslant 0$.

ramp-cliff structures in Sec. V. More discussion can be found in Refs. [33,36].

C. Multifractal detrended fluctuation analysis

DFA was first introduced by Peng *et al.* [14] to study the scaling properties of DNA sequence, in which only the second-order moment $q = 2$ was considered. Later this was generalized into a multifractal version by considering the arbitrary order q, namely multifractal detrended fluctuation analysis (MFDFA) [17,68]. It then became a more common technique for scaling data analysis [14–17,68–74]. For a given discrete time series $x(i)$, $i = 1 \cdots N$, we first estimate its cumulative function:

$$Y(j) = \sum_{i=1}^{j} (x(i) - \overline{x}), \quad j = 1, \cdots N, \tag{19}$$

where $\overline{x}$ is the mean value of x. We then divide it into M_n segments of length n ($n < N$) starting from both the beginning and the end of the time series. Each segment v has its own local trend that can be approximated by fitting a pth-order polynomial P_v^p which is removed from the data. The variances for all the segments v and for all segment lengths n are then calculated by

$$F^2(v,n) = \frac{1}{n} \sum_{j=1}^{n} \left\{ Y[(v-1)n + j] - P_v^p(j) \right\}^2. \tag{20}$$

The qth-order fluctuation function is then defined as

$$F^q(n) = \left(\frac{1}{2M_n} \sum_{v=1}^{2M_n} [F^2(v,n)]^{q/2} \right)^{1/q}. \tag{21}$$

For discussion convenience, we redefine the qth-order fluctuation function as

$$\mathcal{F}_q(n) = F^q(n)^q. \tag{22}$$

In case of scale invariance, we have power law scaling within a significant range of n,

$$\mathcal{F}_q(n) \sim n^{h(q)}, \tag{23}$$

in which $h(q)$ is the corresponding scaling exponent function.

D. Discrete wavelet transform and wavelet leaders

Wavelets have been widely used in data analysis and turbulence research [18–23,25–27,75–77]. Several wavelet-based methods have been proposed by several researchers to extract the scaling exponents from a scaling time series, for example, wavelet coefficients (WC), WTMM [18,19,75], WL [25,26,77], etc. We consider here WC and WL.

The discrete wavelet transform (DWT) is defined as

$$\psi(k,j) = \int_{\mathbb{R}} x(t) \varphi(2^{-j}t - k)\, dt, \tag{24}$$

where φ is the chosen wavelet, $\psi(k,j)$ is the wavelet coefficient, k is the position index, j is the scale index, and $\ell = 2^j$ is the corresponding scale [76,78]. The first way to detect the scale-invariant properties is to consider the wavelet coefficients,

$$Z_q(j) = \langle |\psi(k,j)|^q \rangle \sim 2^{j\tau(q)}, \tag{25}$$

where $\tau(q)$ are the corresponding scaling exponents.

Every discrete wavelet coefficient $\psi(k,j)$ can be associated with the dyadic interval $\varrho(k,j)$,

$$\rho(k,j) = [k\,2^j, (k+1)\,2^j). \tag{26}$$

Thus the wavelet coefficients can be represented as $\psi(\varrho) = \psi(k,j)$. Wavelet leaders are defined as

$$l(k,j) = \sup_{\varrho' \subset 3\varrho(k,j), j' \leqslant j} |\psi(\varrho')|, \tag{27}$$

where $3\varrho(k,j) = \varrho(k-1,j) \cup \varrho(k,j) \cup \varrho(k+1,j)$ [25,28,77]. Thus power law behavior is expected:

$$\mathbb{Z}_q(j) = \langle l(k,j)^q \rangle \sim 2^{j\tau(q)}, \tag{28}$$

in which $\tau(q)$ is the corresponding scaling exponent. Its efficiency has been shown for various types of data set [25–28,77].

Let us recall some previous comparison studies between WTMM, MFDFA, and WL. Oświęcimka *et al.* [68] performed a comparison study between WTMM and MFDFA by analyzing synthesized data. They stated that the MFDFA provides a better estimation of singularity spectrum than WTMM. Jaffard *et al.* [25] stated that WL provides a better singularity spectrum than WTMM. Serrano and Figliola [27] performed a comparison study between MFDFA and WL. They found that WL performs better than MFDFA. However, for a short time series, MFDFA is proposed to extract multifractal spectrum. A detailed comparison can be found in Refs. [25,27,68], respectively, for WTMM and WL, MFDFA and WTMM, and WL and MFDFA.

However, we argue here that DWT violates two facts of the time-frequency representation of a time series. First, the scale of a time series from complex system, for example, turbulent flows, is continuous in a statistical sense, but not discrete on several scales [31,33]. The other one is that for a certain scale, it may not exist all the time [33,38,61]; see also the discussion in the next section. Thus to represent a signal by using a DWT is not consistent with the physical aspect.

III. NONLINEAR EFFECTS

We first consider nonlinear effects by using the classical Duffing equation, which reads

$$\frac{d^2x}{dt^2} + x(1 + \epsilon x^2) = b\cos(\Omega t), \tag{29}$$

in which ϵ is a nonlinear parameter. It can be considered as a pendulum with forcing function $b\cos(\Omega t)$, in which its pendulum length varies with the angle. Figure 1 shows a fifth-order Runge-Kutta numerical solution (thick solid line) with $\epsilon = 1$, $b = 0.1$, $\Omega = 2\pi/25$, and $[x(0), x'(0)] = [1,1]$. The sampling frequency sets as 10 Hz. For comparison, we also show a pure sine wave (thin solid line) with the same mean frequency. One can see that the wave profile of the solution of the Duffing equation is significantly deviating from a sine wave. This deviation is the result of nonlinear interaction,

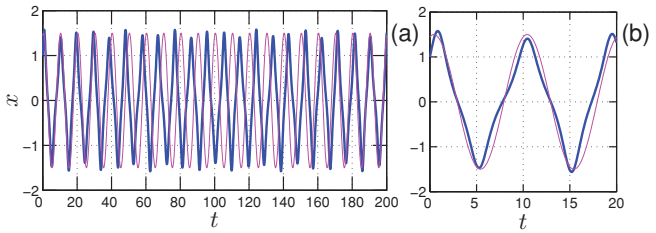

FIG. 1. (Color online) (a) A fifth-order numerical solution (thick solid line) for Duffing equation. (b) An enlarged portion. For comparison, a sine wave with the same mean frequency is also shown as a thin solid line. The departure from a pure sine wave profile is the result of nonlinear interactions, which are nonlinear distortion.

namely nonlinear distortion [38,39]. It is also clearly shown that there are no high-order harmonic components in the physical domain [33]. Figure 2 shows the first three IMF modes obtained from EMD decomposition and the corresponding instantaneous frequency ω from Hilbert spectral analysis. The instantaneous energy is encoded as a color. The instantaneous frequency ω of the first IMF mode is varying within one period. This corresponds to the so-called intrawave-frequency modulation, which is associated with the nonlinear interactions [33,38,39]. It also shows that for a certain frequency, it may not exist clearly all the time.

Figure 3 shows the normalized energy spectra (or the second-order statistical moments) provided by various methods: Fourier analysis (crosses), continuous wavelet transform with db3 wavelet (squares), the first-order DFA (diamonds), SF (triangles), and HSA (solid line). For display convenience, the wavelet, DFA, and SF spectra have been converted from physical domain into frequency domain by taking $f = 1/l$, $f = 1/n$, and $f = 1/\ell$, respectively. We emphasize here that different wavelet families provide a similar spectral curve (not shown here). As pointed out by Huang *et al.* [38] wavelet transform can be considered as an adjustable window

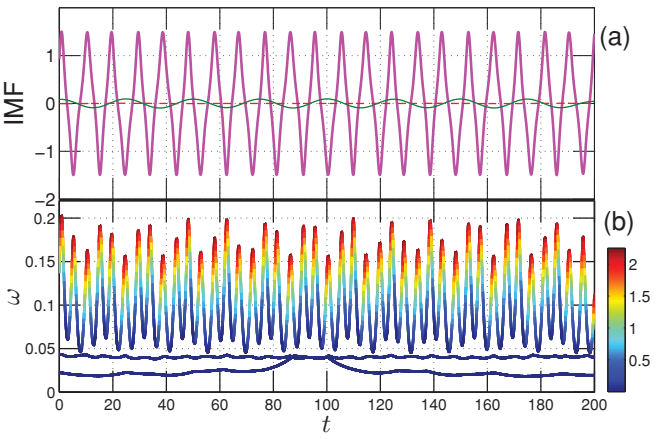

FIG. 2. (Color online) (a) The first three IMF modes from EMD; (b) the corresponding instantaneous frequency ω from Hilbert spectral analysis. Note the variation of the instantaneous frequency within one period. It is an intrawave-frequency modulation, which corresponds to a nonlinear interaction. The instantaneous energy is encoded as a color.

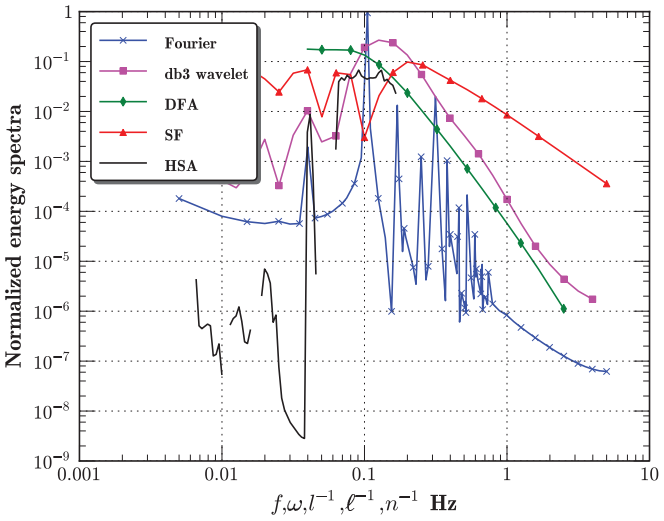

FIG. 3. (Color online) Energy spectra (the second-order statistical moments) provided by various methods: Fourier analysis (crosses), continuous wavelet transform with db3 wavelet (squares), first-order DFA (diamonds), SF (triangles), and Hilbert spectral analysis (solid line). The wavelet, SF, and DFA spectra have been converted into spectral space by taking $f = 1/l$, $f = 1/\ell$, and $f = 1/n$, respectively. Except for the Hilbert-based method, all methods require high-order harmonic components, which are not present in the original signal (see Figs. 1 and 2), to represent this nonlinear process. The high-order harmonics may lead to an artificial energy flux from low frequencies (large scales) to high frequencies (small scales) in spectral space.

Fourier transform. Thus it inherits the shortcomings of the Fourier transform. We observe that except for the Hilbert spectral analysis, all methods require high-order harmonic components to represent this nonlinear process. High-order harmonic components are not present in the time series (see Figs. 1 and 2). It is thus a requirement of the method itself, not the physics [33,38]. This is the main drawback of traditional methods, in which the basis is given *a priori*. Therefore it is inevitable that one requires high-order harmonic components to represent the difference between the analyzed signal and the given basis. We argue here that high-order harmonic components may lead to an artificial energy flux from low frequencies (large scales) to high frequencies (small scales) in spectral space. Therefore, power law behavior, if it exists, may be contaminated by this artificial energy flux. We will show this point experimentally by analyzing a temperature data set with strong ramp-cliff structures in Sec. V.

IV. VALIDATION AND CALIBRATION

In this section, we will validate the Hilbert-based method by performing a comparison study of simulated fBm with Hurst number $H = 1/3$ and synthesized multifractal random walk with an intermittent parameter $\mu = 0.15$. For comparison convenience, spectral curves (or the qth-order statistical moment) provided by SFs, MFDFA, and wavelet are converted from the physical domain into the spectral domain by taking $f = 1/\ell$, $f = 1/n$, and $f = 1/l$, respectively. The corresponding scaling exponents are estimated on the range $0.001 < f < 0.1$ (we set here the sampling frequency as 1). Wavelet transform

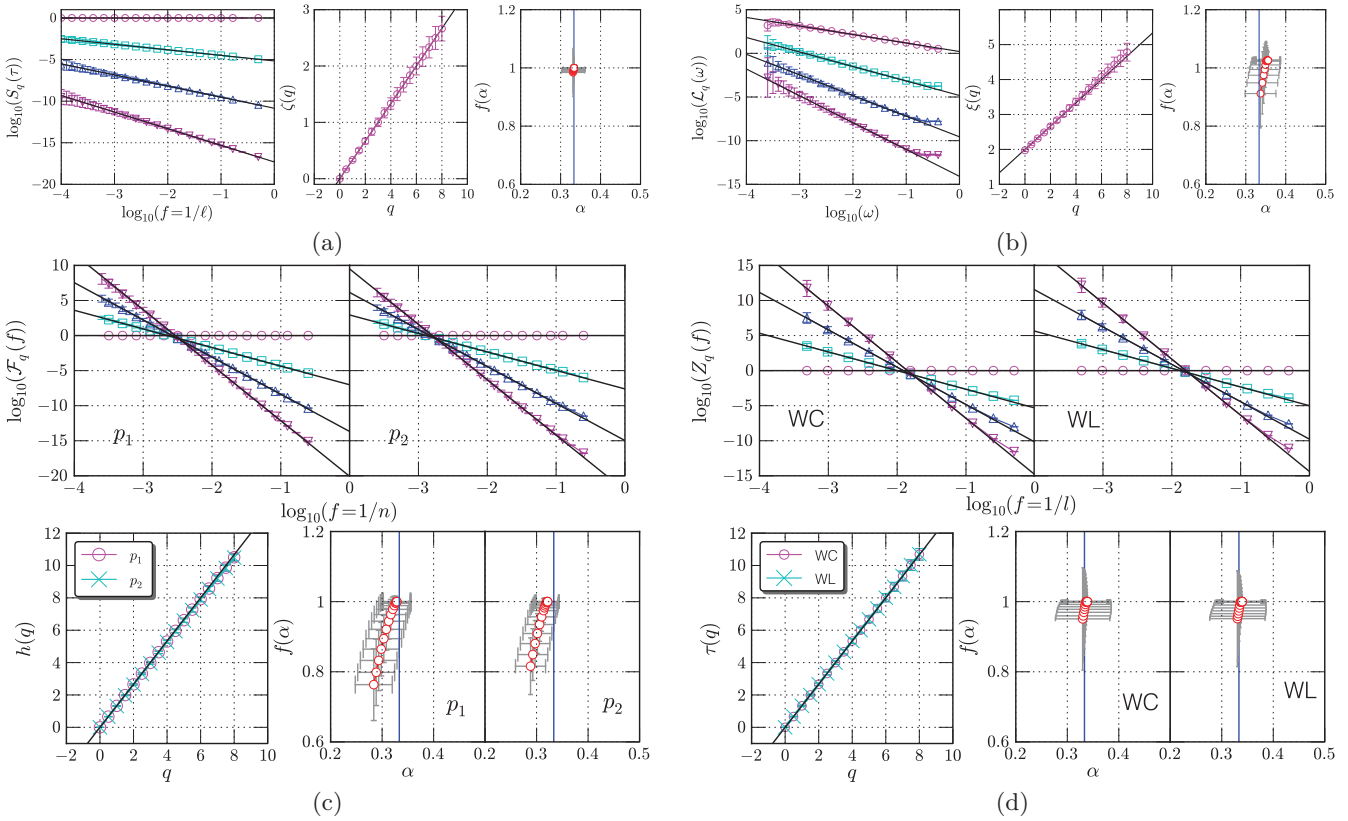

FIG. 4. (Color online) Analysis results of fBm with Hurst number $H = 1/3$. (a) Structure functions. (Left) $S_q(\ell)$ with $q = 0$ (circles), $q = 2$ (squares), $q = 4$ (up-triangles), and $q = 6$ (down-triangles); (middle) the corresponding scaling exponents $\zeta(q)$ on the range $0 \leqslant q \leqslant 8$; (right) the corresponding singularity spectrum $h(\alpha)$. (b) Results of Hilbert spectral analysis. (c) Multifractal detrended fluctuation analysis. (d) Wavelet coefficients and wavelet leaders. The symbols are the same as for structure functions. Scaling exponents are estimated in the range $-3 < \log_{10}(f) < -1$. The statistical errors are estimated from a total of 500 realizations.

is performed by using the db3 wavelet. Due to the limitation of the SF analysis and the HSA, we only consider here the non-negative qth-order moment, $q \geqslant 0$, the left part of the singularity spectrum.

A. Fractional Brownian motion

We have shown in previous works that the arbitrary-order HSA can be applied to the fractional Brownian motion [31,32]. Here we briefly recall these results. FBm is a Gaussian self-similar process with a normal distribution increment, which is characterized by H, the Hurst number $0 < H < 1$ [79–82]. Note that the singularity spectra for the above-mentioned methods are

$$\alpha = \zeta'(q), \quad f(\alpha) = \min_q\{\alpha q - \zeta(q) + 1\}, \tag{30a}$$

for SFs, and

$$\alpha = \xi'(q), \quad f(\alpha) = \min_q\{\alpha q - \xi(q) + 2\}, \tag{30b}$$

for the Hilbert-based method, and

$$\alpha = h'(q) - 1, \quad f(\alpha) = \min_q\{(\alpha + 1)q - h(q) + 1\}, \tag{30c}$$

for DFA, and

$$\alpha = \tau'(q) - 1, \quad f(\alpha) = \min_q\{(\alpha + 1)q - \tau(q) + 1\}, \tag{30d}$$

for WC and WL, respectively. Ideally, we should have $\alpha = H$ and $f(\alpha) = 1$.

We performed 500 realizations each of length 2^{14} data points by applying a Fourier-based Wood-Chan algorithm [83] with $H = 1/3$, which corresponds to the Hurst number of turbulent velocity. We apply the above-mentioned methods to each realization of the data series. The final spectra and statistical errors are then estimated from these 500 realizations. Figure 4 shows results for (a) SF: (left) $S_q(\ell)$ with $q = 0$ (circles), $q = 2$ (squares), $q = 4$ (up-triangles), and $q = 6$ (down-triangles); (middle) the corresponding scaling exponents $\zeta(q)$ on the range $0 \leqslant q \leqslant 8$; (right) the corresponding singularity spectrum $f(\alpha)$, (b) HSA, (c) DFA, and (d) wavelet, respectively. The symbols are the same as the SF symbols. Graphically, all methods provide comparable estimation of $f(\alpha)$. However, we note that the Hilbert-based method slightly overestimates $\xi(q)$ when $q > 6$. Additionally both the first- and second-order DFA provide slight underestimation of $h(q)$ and seem to predict a systematic underestimation of the Hurst number H. The WC and WL provide almost the same estimation for this simple monofractal process. It seems that they provide a better estimation than Hilbert and DFA methods. This result is not in full agreement with Oświęcimka *et al.* [68], who stated that the MFDFA provides a better estimation of H than WTMM.

The above results show that all methods provide comparable prediction of singularity spectra for fBm with $H = 1/3$. However, it seems that SF- and wavelet-based methods provide a better estimation.

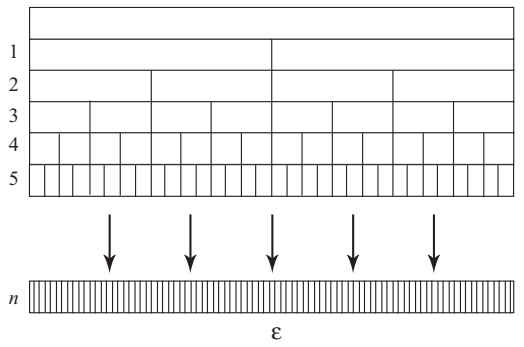

FIG. 5. Illustration of the discrete cascade process. Each step is associated with a scale ratio of 2. After n steps, the total scale ratio is 2^n.

B. Multifractal simulation

We show now that the new method applies to multifractal time series. First, let us consider a multiplicative discrete cascade process to simulate a multifractal measure $\epsilon(x)$. Figure 5 illustrates the cascade process algorithm. The larger scale corresponds to a unique cell of size $L = \ell_0\lambda_1^n$, where ℓ_0 is a fixed scale and $\lambda_1 > 1$ is a dimensional scale ratio. For discrete models, this ratio is often taken as $\lambda_1 = 2$. The models being discrete, the next scale involved corresponds to λ_1 cells, each of size $L/\lambda_1 = \ell_0\lambda_1^{n-1}$. This is iterated and at step p ($1 \leqslant p \leqslant n$) there are λ_1^p cells, each of size $L/\lambda_1^p = \ell_0\lambda_1^{n-p}$. There are n cascade steps, and at step n there are λ_1^n cells, each of size ℓ_0, which is the smallest scale of the cascade. To reach this scale, all intermediate scales have been involved. Finally, at each point the multifractal measure writes as the product of n cascade random variables,

$$\epsilon(x) = \prod_{p=1}^{n} W_{p,x}, \tag{31}$$

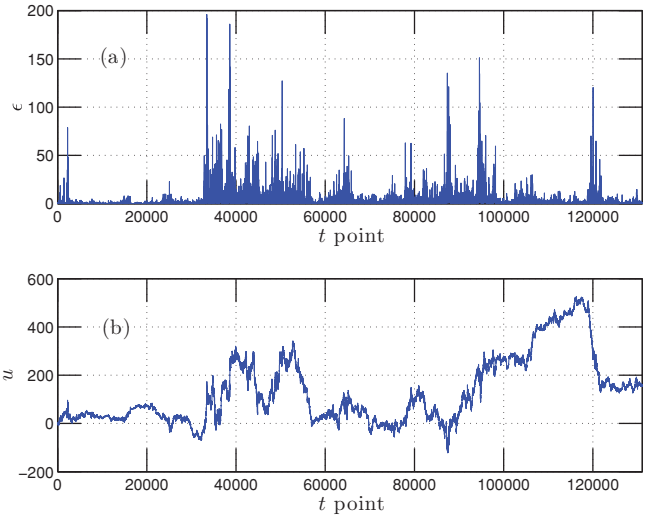

FIG. 6. (Color online) A sample for one realization of length 2^{17} points with $\mu = 0.15$; (a) the multifractal measure, and (b) the constructed multifractal nonstationary process.

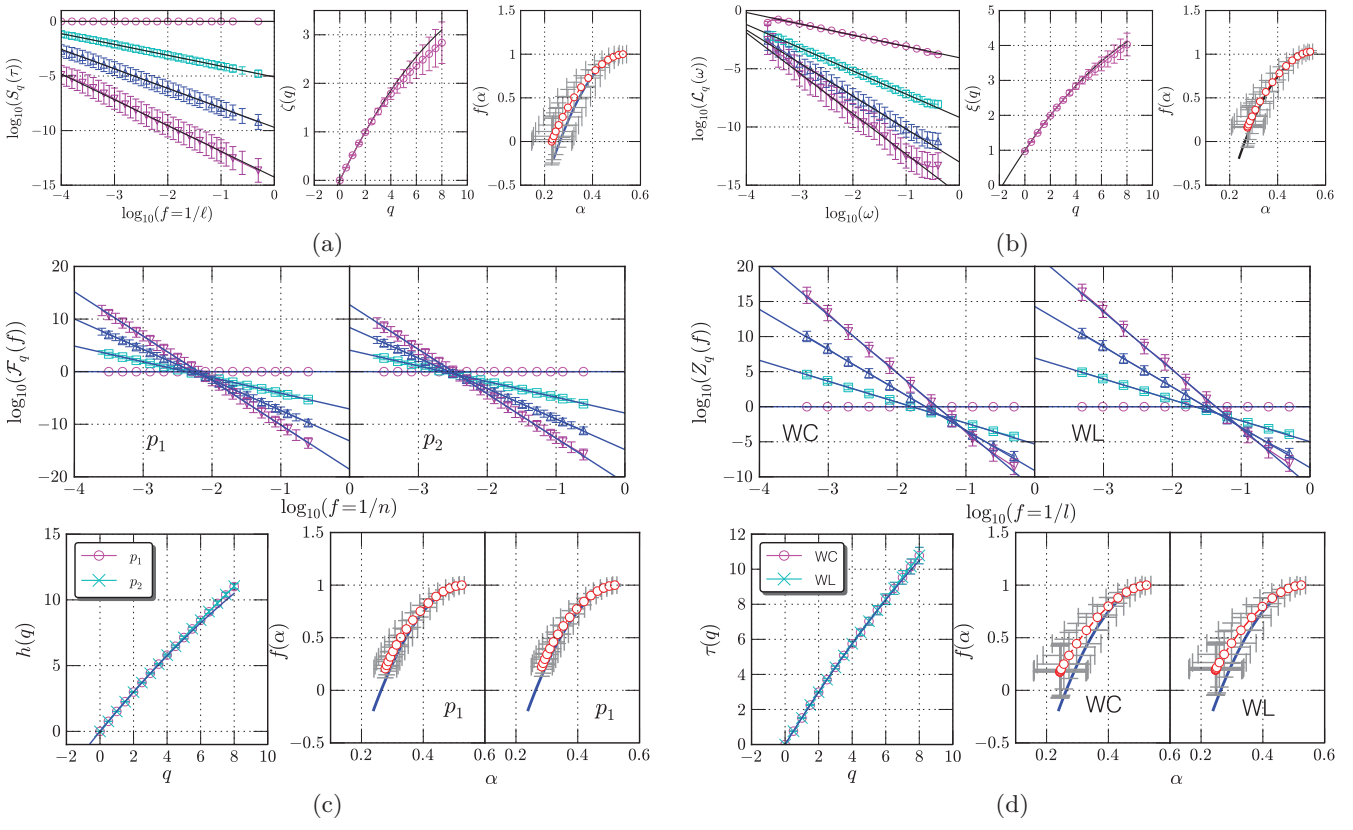

FIG. 7. (Color online) Multifractal random walk with $\mu = 0.15$. (a) Structure function, (b) Hilbert spectral analysis, (c) multifractal detrended fluctuation analysis, and (d) wavelet coefficients and wavelet leaders. The symbols are the same as in Fig. 4. The statistical error bars are estimated from the total 100 realizations.

where $W_{p,x}$ is the random variable corresponding to position x and level p in the cascade [84]. Following multifractal random walk ideas [85,86], we generate a nonstationary multifractal time series as

$$u(x) = \int_0^x \epsilon(x')^{1/2} dB(x'), \tag{32}$$

where $B(x)$ is Brownian motion. Taking lognormal statistic for ϵ, the scaling exponent $\zeta(q)$ such as $\langle |\Delta u_\tau(t)|^q \rangle \sim \tau^{\zeta(q)}$ can be shown to be written as

$$\zeta(q) = \frac{q}{2} - \frac{\mu}{2}\left(\frac{q^2}{4} - \frac{q}{2}\right), \tag{33}$$

where μ is the intermittency parameter ($0 \leqslant \mu \leqslant 1$) characterizing the lognormal multifractal cascade.

Synthetic multifractal time series are generated following Eq. (32). For each realization, we choose $n = 17$ levels, corresponding to data sets with data length 131,072 points each. A sample for one realization is shown in Fig. 6(a) for the multifractal measure and (b) for the nonstationary multifractal time series with $\mu = 0.15$. We perform 100 realizations with intermittent parameter $\mu = 0.15$. Except for the structure functions, we apply all methods to each realization by dividing one realization into eight subsets with 2^{14} data points each. The spectra for each realization are averaged over these eight subsets. The final spectra and error bars are, respectively, ensemble average and standard deviation estimated from these 100 realizations.

Figure 7 shows the results of (a) SF, (b) HSA, (c) MFDFA, and (d) WC and WL, respectively. The symbols are the same as in Fig. 4. The theoretical scaling exponents and the corresponding singularity spectrum $f(\alpha)$ on the range $0 < q < 8$ are shown as a solid line in the corresponding subfigures. We see that SFs underestimate $\zeta(q)$ when $q > 4$. The corresponding estimated singularity spectrum $f(\alpha)$ deviates from the theoretical line when $\alpha < 0.4$, corresponding to $q > 2.5$. It also has the largest statistical error. Hilbert methodology slightly underestimates $\xi(q)$ when $q > 5$. It provides a better estimation of scaling exponents and $f(\alpha)$ than SFs. MFDFA provides the smallest statistical errors for spectral curves $\mathcal{F}_q(n)$, scaling exponents $h(q)$, and singularity spectrum $f(\alpha)$. However, it still slightly overestimates $h(q)$ when $q > 6$. We note that the first- and second-order DFA provide an equivalent result. WC and WL predict almost the same spectral curves, scaling exponents $\tau(q)$ and singularity spectrum $f(\alpha)$. The corresponding singularity spectrum significantly deviates from the theoretical curve. We also note that none of these methods recover the whole theoretical line on the range $0 < q < 8$.

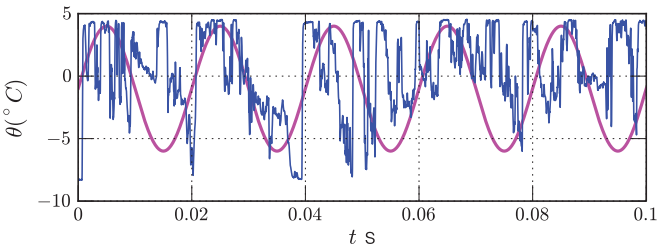

FIG. 8. (Color online) A 0.1-s portion of temperature data showing strong ramp-cliff structures. For comparison, a pure sine wave is also shown as a thick solid line. Note that the ramp-cliff structure is significantly different from a sine wave, which may cause serious artificial energy flux in Fourier spectral space.

V. PASSIVE SCALAR TURBULENCE WITH RAMP-CLIFF STRUCTURES

We now apply the above-mentioned methods to a real time data set, a temperature time series as a turbulent passive scalar. The data are obtained from a jet experiment performed at Joseph Fourier University Grenoble, France. The bulk Reynolds number is about $\mathrm{Re} \simeq 60000$. The corresponding Taylor's microscale Reynolds number is about $\mathrm{Re}_\lambda \simeq 250$. The initial temperature of the two flows are $T_J = 27.8\,^\circ\mathrm{C}$ and $T = 14.8\,^\circ\mathrm{C}$. The measurement location is in the mixing layer and close to the nozzle of the jet. The sampling frequency is 50 kHz. The total data length is 10 s, corresponding to 500,000 data points. Figure 8 shows a 0.1-s portion temperature data, illustrating strong ramp-cliff structures. For comparison, a pure sine wave is also shown. Obviously, the so-called ramp-cliff structure is a large-scale structure with a very sharp interface [87–90]. We note that the profile of ramp-cliff structures is significantly deviating from a sine wave. Thus for the Fourier-based methodologies, it is inevitable that one requires high-order harmonic components to represent their difference, in which the underlying idea is a linear asymptotic approximation [37,38,61]. This linear asymptotic approximation process thus leads to an artificial energy flux from low frequencies (large scales) to higher frequencies (small scales). It means that the Fourier-based spectrum may be

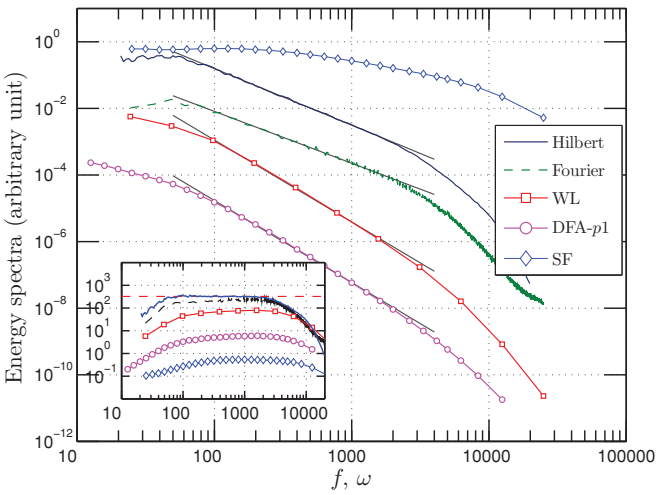

FIG. 9. (Color online) Energy spectra (or the second-order statistical moment) provided by several methods. The inset shows the compensated spectra by multiplying the result by $f^{5/3}$ for Hilbert and Fourier, $f^{8/3}$ for DFA and wavelet, and $f^{2/3}$ for SFs, respectively. For clarity, the curves have been vertically shifted. Both Fourier and Hilbert methods predict a clear power law on the range $80 < \omega < 2000$ Hz. Due to the presence of ramp-cliff structures, the SF analysis fails to capture the power law behavior and DFA and wavelet predict a short inertial range on the range $100 < f < 1000$ Hz. The corresponding scaling exponents are $\beta_\theta = 1.56$ for Fourier, $\xi_\theta(2) = 1.70$ for Hilbert, $\tau_\theta(2) = 2.46$ for WL with db3 wavelet, and $h_\theta(2) = 2.47$ for the first-order DFA, respectively.

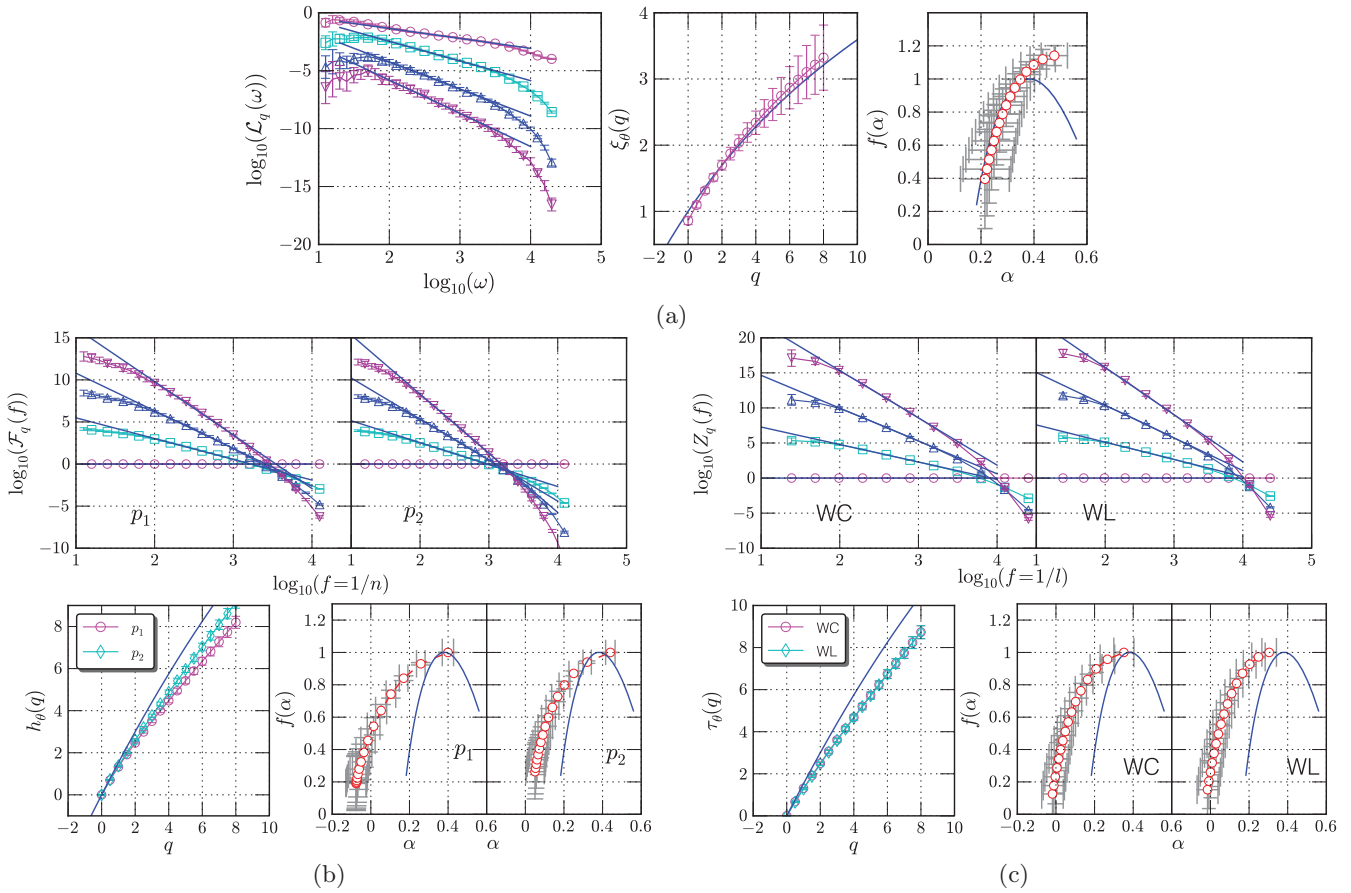

FIG. 10. (Color online) Results for passive scalar (temperature) with strong ramp-cliff (a) Hilbert spectral analysis, (b) multifractal detrended fluctuation analysis, and (c) wavelet coefficients and wavelet leaders. The symbols are the same as in Fig. 4.

contaminated by this artificial energy flux. As another direct consequence, the artificial redistribution of the energy will lead to an unreal correlation if we consider cross-correlation between two scales [91].

The original time series is divided into 122 nonoverlapping segments with 2^{12} data points each. The finally spectra and statistical errors (the standard deviation) are then estimated from these 122 realizations. Figure 9 shows the energy spectra (or the second-order statistical moments) provided by HSA (solid line), Fourier transform (dashed line), WL (squares), the first-order DFA (circles), and SF (diamonds), respectively. The inset shows the corresponding compensated spectra by multiplying a Kolmogorov-Obukhov-Corrsin [92–94] nonintermittent scaling exponent 5/3 for Hilbert spectrum, Fourier power spectrum, 8/3 for WL and DFA, and 2/3 for SF, respectively. Except for the SF, all methods display a clear power law on the range $80 < f < 2000$ Hz or $100 < f < 1000$ Hz, a more than one decade inertial range. The corresponding scaling exponents are $\xi_\theta(2) \simeq 1.70$ for Hilbert, $\beta_\theta \simeq 1.56$ for Fourier, $\tau_\theta(2) \simeq 2.46$ for WL, and $h_\theta(2) \simeq 2.47$ for DFA, respectively, obtained by using a least square fitting algorithm. We note that only the Hilbert-based scaling exponent $\xi_\theta(2)$ is close to the corresponding nonintermittent scaling exponent $\xi_\theta(2) = 5/3$ [36]. It is also comparable with the scaling exponent of longitudinal velocity in fully developed turbulence [2,95,96]. Due to the presence of strong ramp-cliff structures, the SF fails to detect the correct scaling behavior. The influence of large energetic structures on SF has been studied in detail by Huang *et al.* [36] and Huang [33]. It is interesting to note that DFA and WL provide almost the same scaling exponent, which indicates that the ramp-cliff structure may have the same influence on them. We believe that there exists an artificial energy flux as we discussed above in both Fourier and DFA and WL spectra. Thus they may underestimate the scaling exponents [36].

Figure 10 shows the analysis results of (a) Hilbert spectral analysis, (b) MFDFA, and (c) wavelet transform, respectively. The symbols are the same as in Fig. 4. For comparison, the lognormal model of longitudinal velocity [97] is shown as a solid line in the subfigures of scaling exponents and singularity spectra. Due to the failure of SF analysis, we do not present it here (see Ref. [33]). Graphically, these three methodologies predict power law spectra with small statistical error. The corresponding scaling exponents are estimated on the range $80 < f < 2000$ Hz or $100 < f < 1000$ Hz. It is found that the corresponding scaling exponents $\xi_\theta(q)$ and singularity spectrum $f(\alpha)$ are close to the lognormal fitting model, indicating a less intermittent passive scalar turbulence field than what was believed before [36]. MFDFA and wavelets provide comparable statistical errors and singularity spectra. Their scaling exponents and singularity spectra significantly deviate from lognormal model, which is usually considered as evidence that the passive scalar turbulence field is much more intermittent than the velocity field [87–90]. We note that the first- and second-order MFDFA provide different scaling

exponents and singularity spectra, which may be associated with the different abilities of different order polynomials [15,70].

As we already mentioned previously, the wavelet and DFA spectra are strongly influenced by nonlinear large-scale structures (e.g., ramp-cliff structures in passive scalar turbulence). Their scaling exponents are thus contaminated by high-order harmonics. In other words, the statistical property of small scales is contaminated by nonlinear large-scale structures. We believe here that the scaling exponents and singularity spectrum provided by them are not correct. Since the HSA has a very local ability in both physical and spectral spaces, together with the ability of intrawave-frequency modulation for nonlinear processes, the effect of ramp-cliff structures is constrained in the amplitude-frequency space. Therefore, the HSA method may provide a more correct scaling exponent and singularity spectrum. We note that for DFA and the wavelet method, the large deviation from a lognormal spectrum may be interpreted as a shift problem for moment-based methods when the translational invariance is broken [29,30]. It seems that the Hilbert-based method can automatically correct this problem. We also underline here that the Reynolds number of the present passive scalar data set is about $\mathrm{Re}_\lambda \simeq 250$. Thus the strong ramp-cliff structure may be recognized as an effect of the finite Reynolds number. We will address this issue elsewhere.

VI. CONCLUSION

In summary, we introduced in this paper a new method, namely arbitrary-order Hilbert spectral analysis, to characterize scale-invariant properties directly in the amplitude-frequency space [31–33]. It is an extended version of Hilbert-Huang transform [38,39,43]. The main advantage of the Hilbert-based methodology is its fully adaptive [41] and very local ability both in spectral and physical domains [38,39]. Thus, it is not necessary to require high-order harmonics to represent nonlinear and nonstationary processes, which is usually required by conventional Fourier-based methods, such as Fourier transform, wavelet transform, etc. We illustrated the nonlinear effect by using the Duffing equation. It is found that not only Fourier-based methods, but also SF analysis and DFA are influenced by nonlinear processes. It is also found that the HSA can constrain the high-order harmonics by using the intrawave-frequency-modulation mechanism for the nonlinear distortion [38,39,43].

We then performed a comparison study of the Hilbert-based methodology with SF analysis, MFDFA, and WL, by analyzing fBm simulations with Hurst number $H = 1/3$ and a synthesized multifractal lognormal random walk with intermittent parameter $\mu = 0.15$, respectively. For the former simulation, we considered the scaling exponents and singularity spectrum on the range $0 < q < 8$. It was found that all methods provide comparable scaling exponents and singularity spectra. For the latter synthesized multifractal random walk data, HSA and MFDFA provide a better estimation of singularity spectra than SF and WL. However, none of these methods recover the whole spectrum. We finally applied all methods to the passive scalar (temperature) data set with strong ramp-cliff structure, which is an important signature of passive scalar turbulence [88,89]. We found that except for HSA, all the methods require high-order harmonics to represent the ramp-cliff structures. Therefore, the singularity spectra provided by DFA and WL are contaminated by this large nonlinear structure. In fact, it already has been reported by several authors that for passive scalar turbulence the second-order SF and Fourier power spectrum are not consistent with each other [89,98,99]. Warhaft [89] stated that "the reason for this is unclear, but apparently stems from the Fourier transform itself." There is no mathematical transform involved in SF analysis. Now, it seems quite clear that not only Fourier-based methods are strongly influenced by the ramp-cliff structure, but also SF analysis [36] and DFA.

Our experience is that the HSA is a direct measurement of scale-invariant property in the amplitude-frequency space. It thus requires a much larger sample size to get a convergence result than SFs, DFA, and WL. Thus for a sample of small size without large-scale structures, SF analysis, DFA, or WL are useful to extract scaling exponents and singularity spectrum since all methodologies provide almost the same result. In this situation, the HSA is useful to catch the scaling trend. However, if the data set possesses a large-scale structure (e.g., the ramp-cliff structure in passive scalar turbulence, the seasonal cycle in the daily discharge of river flow, etc.), we argue that the HSA is the best choice.

Finally, we would like to provide some comments on the moment-based methods, for example, the methods presented in this work, and the singularity-based approaches (e.g., GMWP [29,30]). Due to the convergence problem, the moment-based methods seem to require a much larger sample size than the singularity-based approaches. Thus the statistical error bars presented in this paper could be nonsignificant due to the finite sample size. Another issue is the right part of the singularity spectrum, which corresponds to evaluating the negative order statistical moments for the moment-based methods. As we already mentioned previously, it may be inaccessible for most of the moment-based methods [30]. However, the singularity-based methods can overcome this problem [29,30]. It seems that the idea of the singularity-based approaches can be extended into the Hilbert frame. This will be presented in a future work.

ACKNOWLEDGMENTS

This work is supported in part by the National Natural Science Foundation of China (Grants No.10772110 and No. 11072139) and the Shanghai Program for Innovative Research Team in Universities. Y.H. was financed in part by a grant from the French Ministry of Foreign Affairs and in part by Université Lille. Y.H. also acknowledges -financial support from EHL of Université Libre de Bruxelles during the preparation of this manuscript. We thank Professor P. Abry from Laboratoire de Physique, CNRS, and ENS, Lyon (France) for providing his wavelet leader codes. The EMD MATLAB codes used in this paper are written by Dr. Gabriel Rilling and Professor Patrick Flandrin from Laboratoire de Physique, CNRS, and ENS, Lyon (France).[2]

[2][http://perso.ens-lyon.fr/patrick.flandrin/emd.html].

[1] F. Anselmet, Y. Gagne, E. J. Hopfinger, and R. A. Antonia, J. Fluid Mech. **140**, 63 (1984).

[2] U. Frisch, *Turbulence: The Legacy of AN Kolmogorov* (Cambridge University Press, Cambridge, 1995).

[3] D. Lohse and K.-Q. Xia, Annu. Rev. Fluid Mech. **42**, 335 (2010).

[4] D. Schertzer and S. Lovejoy, J. Geophys. Res. **92**, 9693 (1987).

[5] F. G. Schmitt, S. Vannitsem, and A. Barbosa, J. Geophys. Res. **103**, 23181 (1998).

[6] M. De Lima and J. Grasman, J. Hydrol. **220**, 1 (1999).

[7] V. Venugopal, S. G. Roux, E. Foufoula-Georgiou, and A. Arnéodo, Phys. Lett. A **348**, 335 (2006).

[8] S. Ghashghaie and Y. Dodge, Nature (London) **381**, 27 (1996).

[9] F. G. Schmitt, D. Schertzer, and S. Lovejoy, Appl. Stoch. Mod. Data Anal. **15**, 29 (1999).

[10] T. Lux, Quantitative Finance **1**, 560 (2001).

[11] L. Calvet and A. Fisher, Review of Economics and Statistics **84**, 381 (2002).

[12] P. Ivanov, A. Bunde, L. Amaral, S. Havlin, J. Fritsch-Yelle, R. Baevsky, H. Stanley, and A. Goldberger, Europhys. Lett. **48**, 594 (1999).

[13] A. S. Monin and A. M. Yaglom, *Statistical Fluid Mechanics, Vol. II* (MIT Press, Cambridge, 1971).

[14] C. K. Peng, S. V. Buldyrev, S. Havlin, M. Simons, H. E. Stanley, and A. L. Goldberger, Phys. Rev. E **49**, 1685 (1994).

[15] K. Hu, P. C. Ivanov, Z. Chen, P. Carpena, and H. E. Stanley, Phys. Rev. E **64**, 11114 (2001).

[16] A. Bashan, R. Bartsch, J. Kantelhardt, and S. Havlin, Physica A **387**, 5080 (2008).

[17] J. Kantelhardt, S. Zschiegner, E. Koscielny-Bunde, S. Havlin, A. Bunde, and H. Stanley, Physica A **316**, 87 (2002).

[18] J. F. Muzy, E. Bacry, and A. Arneodo, Phys. Rev. Lett. **67**, 3515 (1991).

[19] J. F. Muzy, E. Bacry, and A. Arneodo, Phys. Rev. E **47**, 875 (1993).

[20] J. Arrault, A. Arneodo, A. Davis, and A. Marshak, Phys. Rev. Lett. **79**, 75 (1997).

[21] C. Rodrigues Neto, A. Zanandrea, F. Ramos, R. Rosa, M. Bolzan, and L. Sá, Physica A **295**, 215 (2001).

[22] M. Farge, N. Kevlahan, V. Perrier, and E. Goirand, IEEE J. PROC **84**, 639 (1996).

[23] M. Farge, Annu. Rev. Fluid Mech. **24**, 395 (1992).

[24] J. Ghez and S. Vaienti, J. Statist. Phys. **57**, 415 (1989).

[25] S. Jaffard, B. Lashermes, and P. Abry, in *Wavelet Analysis and Applications*, edited by Tao, Mang, and Xu, Applied and Numerical Harmonic Analysis (Birkhäuser Verlag, Basel, Switzerland, 2006), pp. 201–246.

[26] B. Lashermes, S. Roux, P. Abry, and S. Jaffard, Eur. Phys. J. B **61**, 201 (2008).

[27] E. Serrano and A. Figliola, Physica A **388**, 2793 (2009).

[28] B. Lashermes, S. Jaffard, and P. Abry, in *Proceedings of the ICASSP 2005, Philadelphia, March 23, 2005* (IEEE, Philadelphia, USA, 2005).

[29] O. Pont, A. Turiel, and C. J. Pérez-Vicente, Phys. Rev. E **74**, 061110 (2006).

[30] A. Turiel, C. J. Pérez-Vicente, and J. Grazzini, J. Comput. Phys. **216**, 362 (2006).

[31] Y. Huang, F. G. Schmitt, Z. Lu, and Y. Liu, Europhys. Lett. **84**, 40010 (2008).

[32] Y. Huang, F. G. Schmitt, Z. Lu, and Y. Liu, Trait. Signal **25**, 481 (2008).

[33] Y. Huang, Ph.D thesis, Université des Sciences et Technologies de Lille–Lille 1, France, and Shanghai University, China, 2009 [http://tel.archives-ouvertes.fr/tel-00439605/fr].

[34] F. G. Schmitt, Y. Huang, Z. Lu, Y. Liu, and N. Fernandez, J. Mar. Sys. **77**, 473 (2009).

[35] Y. Huang, F. G. Schmitt, Z. Lu, and Y. Liu, J. Hydrol. **373**, 103 (2009).

[36] Y. X. Huang, F. G. Schmitt, Z. M. Lu, P. Fougairolles, Y. Gagne, and Y. L. Liu, Phys. Rev. E **82**, 26319 (2010).

[37] L. Cohen, *Time-Frequency Analysis* (Prentice Hall, Englewood Cliffs, 1995).

[38] N. E. Huang, Z. Shen, S. R. Long, M. C. Wu, H. H. Shih, Q. Zheng, N. Yen, C. C. Tung, and H. H. Liu, Proc. R. Soc. London A **454**, 903 (1998).

[39] N. E. Huang, Z. Shen, and S. R. Long, Annu. Rev. Fluid Mech. **31**, 417 (1999).

[40] G. Rilling, P. Flandrin, and P. Gonçalvès, in *IEEE-EURASIP Workshop on Nonlinear Signal and Image Processing, Grado, Italy, June 8–11, 2003* (IEEE, Grado, Italy, 2003).

[41] P. Flandrin and P. Gonçalvès, Int. J. Wavelets, Multires. Info. Proc. **2**, 477 (2004).

[42] N. E. Huang, M. L. Wu, S. R. Long, S. S. P. Shen, W. Qu, P. Gloersen, and K. L. Fan, Proc. R. Soc. London A **459**, 2317 (2003).

[43] N. E. Huang, in *Hilbert-Huang Transform and Its Applications* (World Scientific, Singapore, 2005), Chap. 1, pp. 1–26.

[44] P. A. Hwang, N. E. Huang, and D. W. Wang, Appl. Ocean Res. **25**, 187 (2003).

[45] A. D. Veltcheva and C. G. Soares, Appl. Ocean Res. **26**, 1 (2004).

[46] J. C. Echeverria, J. A. Crowe, M. S. Woolfson, and B. R. Hayes-Gill, Med. Biol. Eng. Comput. **39**, 471 (2001).

[47] R. Balocchi, D. Menicucci, E. Santarcangelo, L. Sebastiani, A. Gemignani, B. Ghelarducci, and M. Varanini, Chaos Solitons Fractals **20**, 171 (2004).

[48] V. I. Ponomarenko, M. D. Prokhorov, A. B. Bespyatov, M. B. Bodrov, and V. I. Gridnev, Chaos Solitons Fractals **23**, 1429 (2005).

[49] N. E. Huang, M. L. Wu, W. Qu, S. R. Long, and S. S. P. Shen, Appl. Stoch. Model Bus. **19**, 245 (2003).

[50] K. T. Coughlin and K. K. Tung, Adv. Space Res. **34**, 323 (2004).

[51] I. M. Jánosi and R. Müller, Phys. Rev. E **71**, 56126 (2005).

[52] M. K. I. Molla, M. S. Rahman, A. Sumi, and P. Banik, Discrete Dyn. Nat. Soc. **2006**, 45348 (2006).

[53] J. Solé, A. Turiel, and J. Llebot, Nat. Hazard Earth Sys. Sci. **7**, 299 (2007).

[54] Z. Wu, N. E. Huang, S. R. Long, and C. Peng, PNAS **104**, 14889 (2007).

[55] C. H. Loh, T. C. Wu, and N. E. Huang, BSSA **91**, 1339 (2001).

[56] J. Chen, Y. L. Xu, and R. C. Zhang, J. Wind Eng. Ind. Aerodyn. **92**, 805 (2004).

[57] S. J. Loutridis, Appl. Acoust. **66**, 1399 (2005).

[58] F. G. Schmitt, Y. Huang, Z. Lu, S. B. Zongo, J. C. Molinero, and Y. Liu, in *Nonlinear Dynamics in Geosciences*, edited by A. Tsonis and J. Elsner (Springer, New York, 2007), pp. 261–280.

[59] P. Flandrin, G. Rilling, and P. Gonçalvès, IEEE Signal Process. Lett. **11**, 112 (2004).

[60] S. R. Long, N. E. Huang, C. C. Tung, M. L. Wu, R. Q. Lin, E. Mollo-Christensen, and Y. Yuan, IEEE Geoscience and Remote Sensing Soc. Lett. **3**, 6 (1995).

[61] P. Flandrin, *Time-Frequency/Time-Scale Analysis* (Academic Press, Salt Lake City, 1998).
[62] G. Rilling and P. Flandrin, in IEEE International Conference on Acoustics, Speech and Signal Processing, 2006. ICASSP 2006 Proceedings, **3**, 444 (2006).
[63] G. Rilling and P. Flandrin, IEEE Trans. Signal Process (2008).
[64] G. Rilling and P. Flandrin, Adv. Adapt. Data Anal. **1**, 43 (2009).
[65] D. Schertzer, S. Lovejoy, F. G. Schmitt, Y. Chigirinskaya, and D. Marsan, Fractals **5**, 427 (1997).
[66] J. Schmittbuhl, F. G. Schmitt, and C. Scholz, J. Geophys. Res. **100**, 5953 (1995).
[67] F. G. Schmitt, S. Lovejoy, and D. Schertzer, Geophys. Res. Lett. **22**, 1689 (1995).
[68] P. Oświęcimka, J. Kwapień, and S. Drożdż, Phys. Rev. E **74**, 16103 (2006).
[69] C. Heneghan and G. McDarby, Phys. Rev. E **62**, 6103 (2000).
[70] Z. Chen, P. C. Ivanov, K. Hu, and H. E. Stanley, Phys. Rev. E **65**, 041107 (2002).
[71] E. Koscielny-Bunde, J. Kantelhardt, P. Braun, A. Bunde, and S. Havlin, J. Hydrol. **322**, 120 (2006).
[72] M. Sadegh Movahed, G. R. Jafari, F. Ghasemi, S. Rahvar, and M. Rahimi Tabar, J. Stat. Mech. (2006) 02003.
[73] J. Bardet and I. Kammoun, IEEE Trans. Inf. Theory **54**, 2041 (2008).
[74] Q. Zhang, C. Xu, Y. Chen, and Z. Yu, Hydrol. Process. **22**, 4997 (2008).
[75] S. Mallat and W. Hwang, IEEE Trans. Inf. Theory **38**, 617 (1992).
[76] S. Mallat, *A Wavelet Tour of Signal Processing* (Academic Press, Salt Lake City, 1999).
[77] H. Wendt, P. Abry, and S. Jaffard, IEEE Signal Processing Mag. **24**, 38 (2007).
[78] I. Daubechies, Ten Lectures on Wavelets (SIAM, Philadelphia, 1992).
[79] J. Beran, Statistics for Long-Memory Processes (CRC Press, Baca Raton, 1994).
[80] L. Rogers, Math. Finance **7**, 95 (1997).
[81] P. Doukhan, M. Taqqu, and G. Oppenheim, *Theory and Applications of Long-Range Dependence* (Birkhauser, New York, 2003).
[82] C. W. Gardiner, *Handbook of Stochastic Methods*, 3rd ed. (Springer, Berlin, 2004).
[83] A. Wood and G. Chan, J. Comput. Graph. Stat. **3**, 409 (1994).
[84] F. G. Schmitt, Eur. Phys. J. B **34**, 85 (2003).
[85] E. Bacry, J. Delour, and J. F. Muzy, Phys. Rev. E **64**, 026103 (2001).
[86] J. F. Muzy and E. Bacry, Phys. Rev. E **66**, 056121 (2002).
[87] K. Sreenivasan, Proc. R. Soc. London A **434**, 165 (1991).
[88] B. Shraiman and E. Siggia, Nature (London) **405**, 639 (2000).
[89] Z. Warhaft, Annu. Rev. Fluid Mech. **32**, 203 (2000).
[90] A. Celani, A. Lanotte, A. Mazzino, and M. Vergassola, Phys. Rev. Lett. **84**, 2385 (2000).
[91] Y. Huang, F. G. Schmitt, and Y. Gagne, Phys. Rev. Lett. (to be published).
[92] A. N. Kolmogorov, Dokl. Akad. Nauk SSSR **30**, 301 (1941).
[93] A. Obukhov, Izv. Acad. Nauk. SSSR, Geogr. Geofiz. **13**, 58 (1949).
[94] S. Corrsin, J. Appl. Phys. **22**, 469 (1951).
[95] Z. S. She and E. Lévêque, Phys. Rev. Lett. **72**, 336 (1994).
[96] W. van de Water and J. A. Herwijer, J. Fluid Mech. **387**, 3 (1999).
[97] F. G. Schmitt, Physica A **368**, 377 (2006).
[98] R. A. Antonia, E. J. Hopfinger, Y. Gagne, and F. Anselmet, Phys. Rev. A **30**, 2704 (1984).
[99] G. Ruiz-Chavarria, C. Baudet, and S. Ciliberto, Physica D **99**, 369 (1996).